The bottomonium spectrum from the static potential

Master thesis

Michelle Weber

Institut für Theoretische Physik,
Goethe-Universität
Frankfurt am Main

März 2017

Supervisor: Prof. Dr. Marc Wagner
Second supervisor: Dr. Felix Karbstein
(Friedrich Schiller-Universität Jena)

Abstract

In this work a static quark-antiquark potential that is valid for all quark-antiquark separations is constructed. By matching the long range results from lattice QCD to a short range perturbative part we get a continuous potential expression. The lattice part is obtained by fitting an analytic potential model to lattice data for different lattice spacings a. Extrapolating the fitting parameters to the continuum results in a continuum version of the lattice potential.
As an application, the combined quark-antiquark potential is used to determine the bottomonium spectrum in the static limit.

Zusammenfassung

In dieser Arbeit wird ein Ausdruck für das statische Quark-Antiquark Potential konstruiert, der im gesamten Abstandsbereich gültig ist. Dies geschieht, indem das Gitter-Potential, welches bei großen Abständen gültig ist, mit einem kurzreichweitigem störungstheoretischem Potential verbunden wird. Um einen Ausdruck für das Gitter-Potential zu erhalten, wird ein analytisches Modell an Gitterdaten zu unterschiedlichen Gitterabständen gefittet. Durch eine Kontinuumsextrapolation der Fitparameter erhalten wir einen Potentialausdruck im Kontinuum.
Als Anwendung des kombinierten Potentials wird das Bottomonium Spektrum im statischen Grenzwert berechnet.

Contents

1 Introduction

The static potential $V(r)$ between a quark Q and an antiquark $\overline{Q}$ is of fundamental interest in Quantum Chromodynamics (QCD). It is a common observable that has been studied for many years and offers a wide range of applications. By definition the potential describes the interaction energy of an infinitely heavy $Q\overline{Q}$ pair as a function of the distance r. Empirically it is separated into a part, that behaves Coulomb-like ($\sim 1/r$), and a linearly rising term $\sim \sigma r$ at long distances with the so-called string-tension σ. The latter part is responsible for confinement, the fact that quarks cannot be isolated. Trying to separate the $Q\overline{Q}$ pair increases the energy until it is energetically favourable to form a new quark-antiquark pair. This process is known as string breaking.
The theoretical description of the static potential is within QCD, the established fundamental theory of strong interactions. The fact that QCD is asymptotically free, which means that quarks interact weakly at high energies (corresponding to short distances), allows a perturbative treatment in this area with a small coupling constant α_s. In the low-energy regime, which is of particular interest due to confinement, perturbation theory fails. At this point lattice QCD, which is formulated on a discretized spacetime, offers a numerical treatment. In this work the static potential will be applied to describe quarkonium, a non-relativistic bound system.

Quarkonium systems are composed of a heavy quark and its antiquark which are bound by strong interaction. Quarkonia belong to the sub-atomic particle class of mesons. Heavy quarkonia are of special interest because of their properties, which allow an experimental and a non-relativistic theoretical investigation. If the system is constituted of a charm anti-charm pair it is called charmonium $c\bar{c}$, in the case of a bottom and anti-bottom pair one deals with bottomonium $b\bar{b}$. The quarkonium consisting of top anti-top quarks, toponium $t\bar{t}$, does not exist because its large mass leads to a decay even before it could form [1].
This work focuses on bottomonium, which was observed for the first time in 1977 with the detection of $\Upsilon(1S)$. It was also the discovery of the bottom quark itself. To this day, the bottomonium system is of interest and several states, like $\eta_b(3S)$ and most of the D-states, are not confirmed yet. In addition, the $\chi_{bJ}(3P)$ triplet is not completely known. Predictions for these unobserved states exist from theory.
There are two different approaches for a theoretical treatment of quarkonia. The first one is a direct calculation within lattice QCD. Several such calculations exist, but they are complex and time-consuming [1]. The alternative and easier approach uses potential models [2]. We will make use of the latter strategy and use the static $Q\overline{Q}$ potential as an input for the Schrödinger equation, which can then be solved for the quarkonium states. The initial aim of this work is to state an expression for the static $Q\overline{Q}$ potential which is valid through the whole distance range. For that purpose, we have to combine short

range perturbation theory and long range results from lattice QCD. As an application we calculate the experimentally well-known S- and P-states of the bottomonium system in the static limit.

In the following, the structure of this thesis is outlined. First of all, chapter 2 briefly presents lattice calculations. The main focus lies on the construction of a continuum expression for the static potential from lattice QCD. Chapter 3 deals with perturbation theory and collects the most important perturbative formulas, based on [3]. In the next chapter both potentials are merged. Finally, in chapter 5, the bottomonium spectrum is calculated with the combined potential. Results are presented and discussed.

2 Construction of the lattice potential

In this chapter a lattice version of the $Q\overline{Q}$ potential is derived from gauge field ensembles. Configurations for four different lattice spacings for $n_f = 2$ quark flavors, listed in table 1, are available. They were generated by the European Twisted Mass Collaboration (ETMC) [4]. Static potential data for each β, calculated from these configurations already exist. They extend up to a maximal distance of ≈ 0.6 fm. Calculating such precise lattice data with on- and off-axis Wilson loops at higher distances is time-consuming. To describe a full, precise potential and calculate higher excited bottomonium states, more data at larger separations are necessary.
Starting from the gauge field configurations, the $Q\overline{Q}$ potential is calculated again up to slightly larger distances. This time we use only on-axis Wilson loops and thus obtain a few more data points. Another main difference between the data is, that the existing ones come only with APE but without HYP smearing, whereas for the data we calculate both smearing techniques are used (cf. section 2.2). This is done because HYP smearing reduces the errors at larger separations. In order to distinguish between the two data types, we use an index $n \in \{1, 2\}$. $n = 1$ denotes everything that originates from the HYP data and respectively $n = 2$ denotes results from the lattice data without HYP smearing. In the following chapters the details of calculating the static potential and the combination of both data sets is described.

β	a [fm]	$(L/a)^3 \times T/a$	m_{PS} [MeV]	r_0/a	$N_{n,\beta}$
3.90	0.079(3)	$24^3 \times 48$	340(13)	5.36(4)	108/168
4.05	0.063(2)	$32^3 \times 64$	325(10)	6.73(5)	189/71
4.20	0.0514(8)	$24^3 \times 48$	284(5)	8.36(6)	211/123
4.35	0.0420(17)	$32^3 \times 64$	352(22)	9.81(13)	295/146

Table 1: Ensembles of gauge link configurations employed in the present work. $N_{n,\beta}$ is the number of configurations considered for the calculation of the potential with/without HYP smearing.

2.1 Lattice calculations

The lattice discretizes the space-time. Typical parameters, which are listed in table 1, are the spatial (L) and temporal (T) extension of the lattice. The distance between two lattice sites is the lattice spacing a which directly corresponds to the coupling constant β. The quantity r_0 is called the Sommer parameter and is defined via

$$\frac{\mathrm{d}}{\mathrm{d}r}V(r)\bigg|_{r=r_0} r_0^2 = 1.65\ . \tag{2.1}$$

It is a characteristic length scale associated with the quark-antiquark potential $V(r)$ and can be used to determine the lattice spacing.
With the help of the discretization it becomes possible to calculate QCD problems numerically by solving path integrals with Monte Carlo methods.
The first step for computations on the lattice is the definition of a suitable operator. In the case of the quark-antiquark potential the operator

$$\hat{\mathcal{O}} \equiv \overline{Q}(\mathbf{x})U(\mathbf{x},\mathbf{y})Q(\mathbf{y}) \tag{2.2}$$

acting on the QCD vacuum state $|\Omega\rangle$ creates our state of interest: a quark located at $\mathbf{x}$ and an antiquark at $\mathbf{y}$ within a distance of $R = |\mathbf{x}-\mathbf{y}|$. The quarks are static, which means that they are infinitely heavy and therefore cannot move. We investigate the propagation amplitude of this quark-antiquark state $|\phi(R)\rangle = \hat{\mathcal{O}}|\Omega\rangle$ which is called correlation function $\mathcal{C}(T)$ and can be expressed as a path integral:

$$\mathcal{C}(T) = \langle\Omega|\hat{\mathcal{O}}^\dagger(T)\hat{\mathcal{O}}|\Omega\rangle = \frac{1}{Z}\int \mathcal{D}\Psi\mathcal{D}\overline{\Psi}\mathcal{D}A\ \mathcal{O}(T)\mathcal{O}\mathrm{e}^{-S_{QCD}}. \tag{2.3}$$

The integration runs over all possible quark and gauge field configurations. Z is a normalization factor and S_{QCD} denotes the euclidean action. The left hand side of this equation can be modified by using the euclidean time evolution $\hat{\mathcal{O}}(T) = \mathrm{e}^{\hat{H}T}\hat{\mathcal{O}}\mathrm{e}^{-\hat{H}T}$ and inserting a set of energy eigenvalues:

$$\begin{aligned}\langle\Omega|\hat{\mathcal{O}}^\dagger(T)\hat{\mathcal{O}}|\Omega\rangle &= \sum_n \langle\Omega|\mathrm{e}^{\hat{H}T}\hat{\mathcal{O}}^\dagger\mathrm{e}^{-\hat{H}T}|n\rangle\langle n|\hat{\mathcal{O}}|\Omega\rangle \\ &= \sum_n |\langle\phi(R)|n\rangle|^2\mathrm{e}^{-(E_n-E_\Omega)T}.\end{aligned} \tag{2.4}$$

In the limit of large times T, the terms of the higher excited states ($n \geq 1$) are exponentially suppressed. This is the case because the energy differences $E_n - E_\Omega$ increase.
For large T only the ground state term ($n = 0$) contributes and one finds an exponential decay in the correlation function:

$$\mathcal{C}(T) = |\langle\phi(R)|0\rangle|^2\mathrm{e}^{-(E_0-E_\Omega)T}, \quad \text{for } T \gg 1. \tag{2.5}$$

What actually has to be computed is the path integral on the right hand side of equation (2.3). In the special case of the static potential it can be simplified in such a way that the quark fields can be integrated out [5]. What remains is a path integral of the famous Wilson loop $W_C[A]$:

$$\mathcal{C}(T) \propto \frac{1}{Z} \int \mathcal{D}A \; W_C[A] \mathrm{e}^{-S_{\text{eff}}} \equiv W(R,T), \tag{2.6}$$

with an effective action S_{eff} which is independent of quark fields. Figure 1 shows a simple Wilson loop, which is calculated along a closed, rectangular contour C. Combining equations (2.5) and (2.6), we see that the energy $E_0 - E_\Omega$ at distance R can be extracted by fitting an exponential function to the vacuum expectation value of the Wilson loop $\langle W_C[A] \rangle = W(R,T)$:

$$W(R,T) \propto \mathrm{e}^{-(E_0 - E_\Omega)T} \quad \text{for } T \gg 1. \tag{2.7}$$

In practice one uses the effective potential

$$V_{\text{eff}}(R,T) = \frac{1}{a} \ln \left(\frac{W(R,T)}{W(R,T+a)} \right) \tag{2.8}$$

and obtains the static energy $V(R) \equiv E_0 - E_\Omega$ by fitting a constant to the large time part of the curve (2.8). The procedure is illustrated in figure 2.
With the transition to the lattice, the gauge field $A_\mu(x)$ is replaced by link variables U_μ that connect lattice sites, which correspond to a quark field [6]. The Wilson loop takes the following form:

$$W_C[U] = \mathrm{Tr} \prod_{l \in C} U_l. \tag{2.9}$$

It is the trace of a product of link variables U_μ which form a rectangle with one axis in time direction and one in spatial direction.

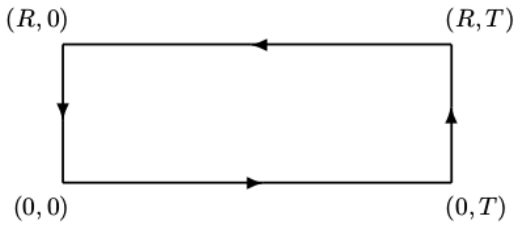

Figure 1: Wilson loop $W(R,T)$ with spatial extension R and temporal extension T (taken from [6]).

So far, we only took into account that the suppression of higher terms at large time separations is important for good numerical results. Taking a look back at equation (2.4) it becomes obvious that it is also necessary to have a large overlap to the ground

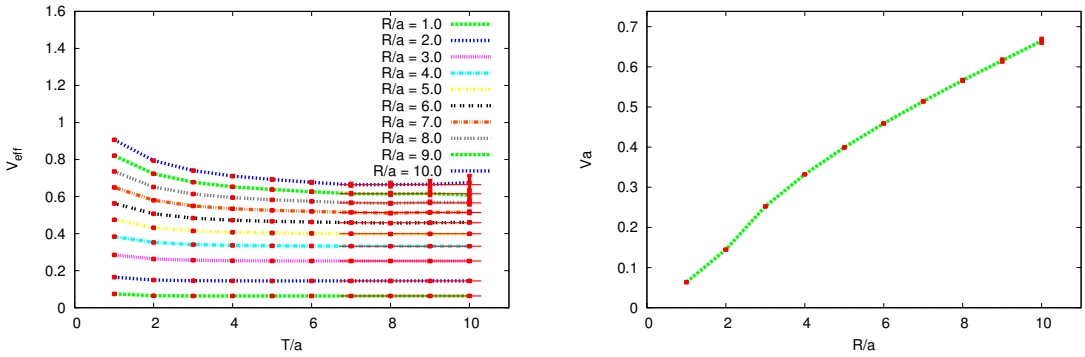

Figure 2: **Left**: Effective potentials $V_{\text{eff}}(R,T)$, with their fits to a constant at large T. **Right**: The resulting static quark-antiquark potential.

state $|\langle\phi(R)|0\rangle|$ compared to the other overlaps. Otherwise the correlation function has no clear signal and one has to do additional, time-consuming calculations to much larger time separations. To guarantee the large overlap, smearing techniques are used.

2.2 Smearing techniques

The common smearing techniques are APE and HYP smearing, from which APE smearing is the easier option. In principle smearing is a transformation which replaces link variables by averages of neighbouring links. This is why smeared links are often called "fat links". The techniques smoothen the gauge field and improve the signal-to-noise ratio of the correlation function.

APE smearing only takes into account spatial links in form of adding a sum of staples $\Sigma_\mu(x)$, weighted by a factor α, to the original link [7]. A staple is a product of three links which connect the original link's endpoints.

$$U_\mu(x) \longrightarrow \mathcal{P}\left\{(1-\alpha)U_\mu(x) + \frac{\alpha}{6}\Sigma_\mu(x)\right\} \tag{2.10}$$

Since the procedure leads out of the gauge group SU(3), the operator $\mathcal{P}$ projects back to the group. A typical value for the weighting factor is $\alpha \approx 0.5$.

HYP smearing further makes use of temporal links. Instead of staples, HYP smearing averages over links within hypercubes attached to the original link [7]. The exact procedure how the hypercubic fat link is constructed in three steps can be studied in [8].

2.3 Jackknife analysis

The jackknife method is a resampling method which is often used to compute the standard error of a data set. Starting from the initial data set, a pseudo-independent set of so called jackknife samples is constructed. To explain the procedure we look at the simple example of a list of N values $\mathbf{X} = (x_1, x_2, ..., x_N)$.
The first step is the construction of the reduced jackknife samples by leaving out one observation x_i from $\mathbf{X}$. So a reduced set of $N-1$ values is left. This is repeated for every other x_i in $\mathbf{X}$, where $i \in \{1, ..., N\}$. What comes out are N different samples $\{\mathbf{X}_{(i)}\}_{i=1...N}$, each of them contains $N-1$ values.
Once we have the samples, the actual analysis can be done. The estimator θ of interest which we want to extract from our data, is calculated on each of the subsamples $\mathbf{X}_{(i)}$. An easy example for θ is the mean value, whose jackknife replication reads

$$\theta_{(i)} = \sum_{j \neq i} \frac{x_j}{N-1}. \tag{2.11}$$

Finally, from the resulting list of N jackknife samples $\{\theta_{(i)}\}_{i=1...N}$ the jackknife error

$$\Delta_\theta = \sqrt{\frac{N-1}{N} \sum_{i=1}^{N} (\theta_{(i)} - \overline{\theta})^2} \tag{2.12}$$

is computed. $\overline{\theta}$ is the result from the full sample. In this work we make use of data for the $Q\overline{Q}$ potential which exist in the following, more involved form: For every lattice spacing we have a full set, which was calculated including all available lattice configurations, and several reduced sets, obtained as described above by leaving out one configuration at a time during the calculation of the potential. Our estimators of interest are the fitting parameters of the potential model α and σ (see equation (2.15) below).
Since we will also work directly with the parameter jackknife samples in the following, we have to consider that the $\theta_{(i)}$ are distributed in a narrower space around the mean value $\overline{\theta}$ than the original data. This becomes obvious when rewriting equation (2.11) to

$$\theta_{(i)} = \overline{x} + \frac{1}{N-1}(\overline{x} - x_i). \tag{2.13}$$

We see that the linear size of the distribution interval is $N-1$ times smaller than that of the original ensemble [9]. To ensure a correct use, the jackknife samples have to be modified with an inflation factor $\sqrt{N-1}$:

$$\theta_{(i)} \to \overline{\theta} + \sqrt{N-1}(\theta_{(i)} - \overline{\theta}). \tag{2.14}$$

A comparison between the distributions of the inflated and uninflated jackknife samples $\theta_{(i)}$ for our special case, where the estimators are parameters fitted to lattice potential data, is shown in figure 3.

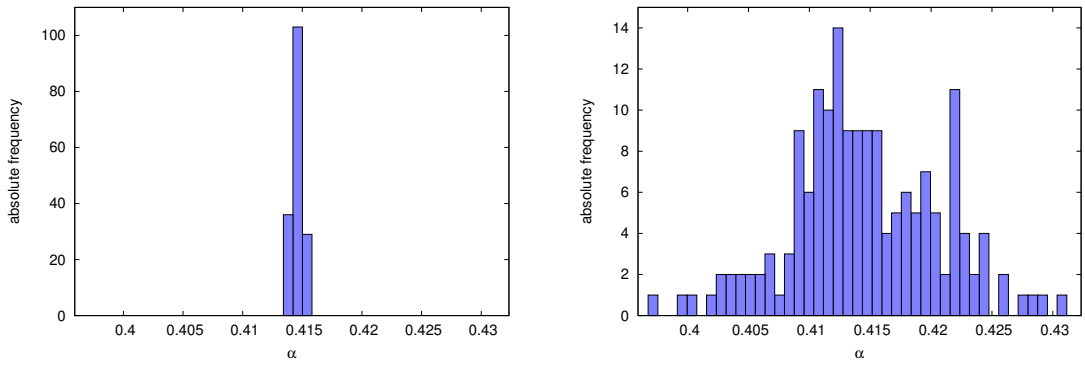

Figure 3: Distribution of the α parameter values for $\beta = 3.9$ and without HYP. The sample size is $N = 168$ and the bin size is 0.0008.
Left: Initial parameter values obtained by fits to the reduced samples.
Right: Inflated values, modified according to equation (2.14).

2.4 Continuum extrapolation

2.4.1 General approach and correlations

The main purpose in the following is to combine the different lattice potential data with HYP ($n = 1$) and without HYP smearing ($n = 2$) to state a final result in the continuum. The combination is done in two main steps: a continuum extrapolation of the fitting parameters, where both data types can be treated independently, with a following weighting of the results in the continuum.
The extrapolation is done for both data in the same way. For every lattice spacing a there are several but not the same number of reduced samples $N_{n,\beta}$ with values for the $Q\overline{Q}$ potential. The very first step is to fit the potential model

$$V(r) = V_0 - \frac{\alpha}{r} + \sigma r, \tag{2.15}$$

which is often called the Cornell potential, to all of these data sets. For details on the fitting procedure see also section 2.4.2. The energy constant V_0 is physically not important and can be neglected after the fit. Thus, for every lattice spacing and n we get a list of pairs of fitting parameters $\{(\alpha_{n,i}, \sigma_{n,i})\}_{i=1\ldots N_{n,\beta}}$. Before going on, these values have to be corrected with the inflation factor as described in the jackknife section above.
We have to keep in mind, that the two parameters from one fit, such as $(\alpha_{1,8}, \sigma_{1,8})$ for $\beta = 3.9$, are correlated. We intend to maintain these correlations during the following procedure and to have only few losses in the continuum. This is important because otherwise information is lost and the continuum result is less meaningful. Before proceeding

any further, we check the initial correlations by calculating

$$\mathrm{corr}(\alpha_n, \sigma_n) = \sum_{i=1}^{N_{n,\beta}} \frac{(\alpha_{n,i} - \overline{\alpha}_n)(\sigma_{n,i} - \overline{\sigma}_n)}{\sqrt{\mathrm{var}(\alpha_n)\mathrm{var}(\sigma_n)}}. \tag{2.16}$$

Dividing by the variances

$$\mathrm{var}(\alpha_n) = \frac{1}{N_{n,\beta} - 1} \sum_{i=1}^{N_{n,\beta}} (\alpha_{n,i} - \overline{\alpha}_n)^2 \qquad \mathrm{var}(\sigma_n) = \frac{1}{N_{n,\beta} - 1} \sum_{i=1}^{N_{n,\beta}} (\sigma_{n,i} - \overline{\sigma}_n)^2 \tag{2.17}$$

ensures the normalization, so that $-1 \leq \mathrm{corr}(\alpha, \sigma) \leq +1$. A correlation of $+1$ corresponds to a perfect positive correlation between the parameters, which means that if $\alpha_{n,i}$ increases/decreases, $\sigma_{n,i}$ increases/decreases as well. Respectively, a correlation of -1 indicates a perfect negative correlation, an increase of $\alpha_{n,i}$ implies a decrease of $\sigma_{n,i}$ and vice versa. If $\mathrm{corr}(\alpha, \sigma) = 0$ there is no correlation between the parameters.
Table 2 lists the initial correlations immediately after the fits at different lattice spacings and for both data sets, with and without HYP smearing. Obviously, all correlations are very close to -1, so we clearly have a negative correlation. This is exactly what we expect, because for an increased value of σ the slope of the potential increases as well, which needs to be compensated by a decreased value of α. Figure 4 illustrates the correlation between the parameters.
During the investigations we also studied other fitting models with more parameters than the Cornell potential (2.15) to model the lattice data. Motivated by perturbation theory, we investigated the addition of logarithmic terms $\frac{\ln^m(r/r_0)}{r}$. Three more models

$$V^{(M)}(r) \quad = \quad V_0 - \frac{\alpha}{r} + \sigma r + \sum_{m=1}^{M} \gamma_m \frac{\ln^m(\frac{r}{r_0})}{r}, \quad M = 1, 2, 3 \tag{2.18}$$

were considered. The results for adding two more ($M = 2$) or three more ($M = 3$) terms were not satisfying for our intention of the continuum extrapolation. The γ parameters at different lattice spacings, especially γ_2 and γ_3, differed so much that an extrapolation was not meaningful. For $M = 1$ we found a linear dependence of γ_1 from a^2, but still decided not to use this model because the continuum value $\gamma_{1,c}$ is close to zero and even agrees with zero in its large uncertainty. Moreover the χ^2_{red} values of those fits were too small, which is an evidence for overfitted data. Apparently, the standard "Coulomb plus linear" model is already sufficient to describe the $Q\overline{Q}$ lattice potential data.

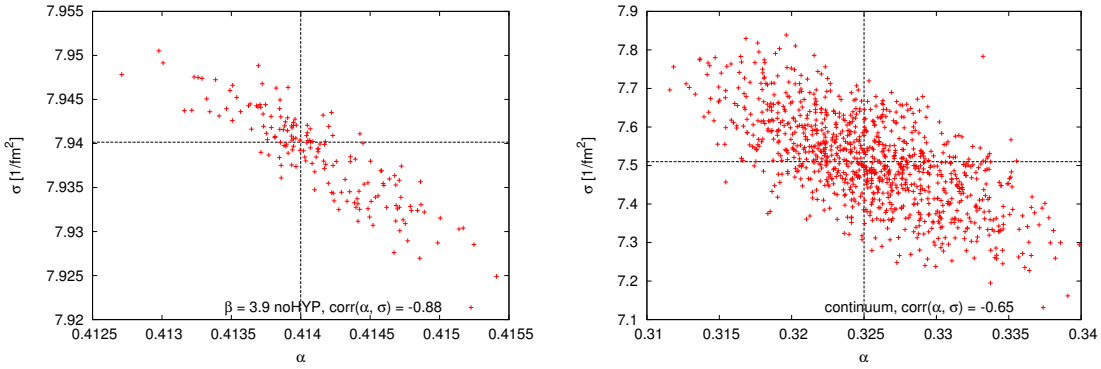

Figure 4: Illustration of the correlations.
Left: Covariance ellipse for data without HYP and $\beta = 3.9$. The shape is typical of a negative correlation, most of the points are located in the second and fourth quadrant.
Right: Covariance ellipse in the continuum. 1000 cohesive parameter pairs are plotted.

2.4.2 Fitting procedure

In the previous section we already mentioned the fitting as the very first step and explained that we will use only equation (2.15) to model the lattice data. For that we use a standard χ^2 minimizing fit. Up next, we introduce the details of the fitting procedure. The fitting range can be restricted through r_{min} and r_{max}. Since we want to use all data at long distances, r_{max} is always set to the maximal available distance. In order to ensure that $\chi^2_{\text{red}} \lesssim 1$, which is an evidence for a good fit, r_{min} can still be adjusted. Because of lattice discretization errors at small distances $r < 2a$, the minimal fitting point should be larger. Additionally, for HYP data $r_{\text{min}} > 3a$ because of uncertainties that come with the smearing in this range. Another criterion for the choice of r_{min} is that the resulting fit parameters from data with HYP and without HYP have to coincide in a certain error range. This is important when combining both data later. With a large deviation of the respective parameters the weighting would be problematic. Finally, one has to balance between a good fit and a sufficient overlap of the parameters. Table 2 lists the chosen fitting ranges based on the above conditions and the corresponding χ^2_{red} values. Moreover the mean values and jackknife errors for α and σ are included. A typical fit to lattice data is shown in figure 5.

β		$r_{\min} - r_{\max}$	χ^2_{red}	$\alpha \pm \Delta\alpha$	$\sigma \pm \Delta\sigma$ [1/fm^2]	corr(α, σ)
3.90	HYP	$3a - 10a$	0.34	0.415 ± 0.015	7.31 ± 0.19	-0.96
	noHYP	$2.83a - 8a$	0.36	0.414 ± 0.006	7.94 ± 0.09	-0.88
4.05	HYP	$3a - 10a$	1.78	0.391 ± 0.008	7.39 ± 0.15	-0.96
	noHYP	$2.83a - 8a$	0.53	0.386 ± 0.006	7.87 ± 0.08	-0.89
4.20	HYP	$4a - 12a$	0.12	0.382 ± 0.011	7.41 ± 0.18	-0.92
	noHYP	$2.83a - 10a$	0.66	0.368 ± 0.006	7.60 ± 0.10	-0.76
4.35	HYP	$4a - 14a$	0.22	0.353 ± 0.007	7.55 ± 0.15	-0.93
	noHYP	$3a - 10a$	0.7	0.347 ± 0.004	7.86 ± 0.09	-0.85

Table 2: Summary of all relevant parameters before the continuum extrapolation. The errors $\Delta\sigma$ do not include lattice errors so far.

	$\alpha \pm \Delta\alpha$	$\sigma \pm \Delta\sigma$ [1/fm^2]	corr(α, σ)
HYP	0.331 ± 0.011	7.56 ± 0.23	-0.73
noHYP	0.324 ± 0.006	7.50 ± 0.14	-0.61
combined	0.325 ± 0.005	7.51 ± 0.12	-0.65

Table 3: Continuum parameters.

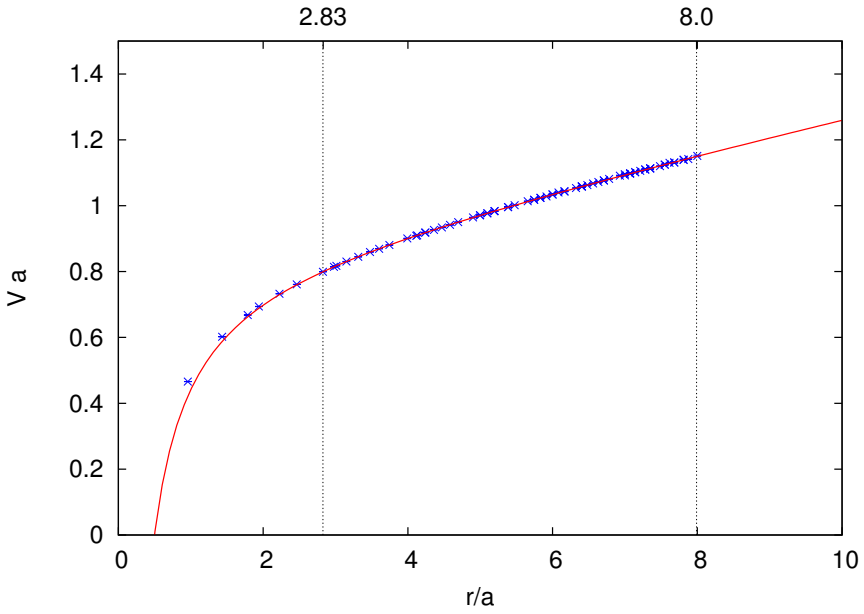

Figure 5: An example of a fit for $\beta = 3.9$ and data without HYP smearing. The fitting area is restricted by r_{min} and r_{max}.

2.4.3 Extrapolation

For our aim to state a continuum version of the lattice potential we perform an extrapolation. Continuum extrapolations are often done by randomly resampling with a gaussian distribution, fitting linear functions to the data points and thus generating parameter lists in continuum. In our case this approach would separate the (α, σ) pairs and thus lose their correlation. Due to this, the extrapolation is done directly with the inflated fitting parameters $\{(\alpha_{n,i}, \sigma_{n,i})\}_{i=1\ldots N_{n,\beta}}$ from the jackknife samples.
We have to consider that σ is dimensionful and thus depends on the lattice spacing a, which has an error Δa. This leads to an additional error which we have to take into account in our computation by adding both errors quadratically:

$$\Delta\sigma \to \sqrt{(\Delta\sigma)^2 + \left(\frac{\sigma \Delta a}{a}\right)^2}. \tag{2.19}$$

Randomly, four pairs of $(\alpha_{n,i}, \sigma_{n,i})_\beta$, one per lattice spacing, are chosen. There is a linear dependence between the parameters and the squared lattice spacing a^2. With the fit of a linear function to the four data points we get a value for α, σ respectively, in the continuum where $a^2 \to 0$. For a good statistics it should be enough to repeat this 1000 times and hence generate 1000 pairs $\{(\alpha_{n,i}, \sigma_{n,i})_c\}_{i=1\ldots1000}$ in the continuum. Mean values $\overline{\alpha}_n, \overline{\sigma}_n$ and standard errors $\Delta\alpha_n, \Delta\sigma_n$ yield the continuum results for the data sets

with HYP and without HYP. Figure 6 illustrates the extrapolation processes which are done for both data sets independently.

2.4.4 Weighting

The last step is the combination of the resulting fitting parameters from data with HYP and without HYP. For that we take the two continuum lists of pairs $\{(\alpha_{1,i}, \sigma_{1,i})_c\}_{i=1...1000}$ and $\{(\alpha_{2,i}, \sigma_{2,i})_c\}_{i=1...1000}$ and weight the parameters so that we get a final list of continuum parameters $\{(\alpha_i, \sigma_i)\}_{i=1...1000}$. The weighting is simply done by fitting a constant α_i to two points $\alpha_{1,i}$ and $\alpha_{2,i}$ (σ_i respectively):

$$\alpha_i = \frac{\frac{1}{\Delta\alpha_1^2}}{\frac{1}{\Delta\alpha_1^2}+\frac{1}{\Delta\alpha_2^2}}\alpha_{1,i} + \frac{\frac{1}{\Delta\alpha_2^2}}{\frac{1}{\Delta\alpha_1^2}+\frac{1}{\Delta\alpha_2^2}}\alpha_{2,i} \ , \tag{2.20}$$

$$\sigma_i = \frac{\frac{1}{\Delta\sigma_1^2}}{\frac{1}{\Delta\sigma_1^2}+\frac{1}{\Delta\sigma_2^2}}\sigma_{1,i} + \frac{\frac{1}{\Delta\sigma_2^2}}{\frac{1}{\Delta\sigma_1^2}+\frac{1}{\Delta\sigma_2^2}}\sigma_{2,i} \ . \tag{2.21}$$

Now we can investigate the correlations again. Optimally there should not be much difference compared to the inital ones. Indeed we get a final value of $\mathrm{corr}(\alpha, \sigma) = -0.65$, which is slightly less than before. The loss is attributed to the addition of the lattice spacing errors. Nevertheless the value still shows an obvious negative correlation (cf. figure 4). Figure 7 illustrates the combination. Moreover table 3 lists the continuum results.

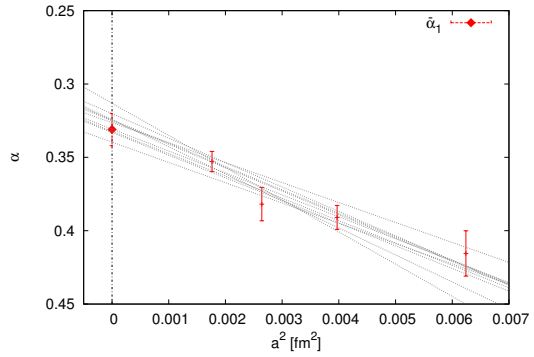

(a) HYP, $\overline{\alpha}_1 = 0.331 \pm 0.011$

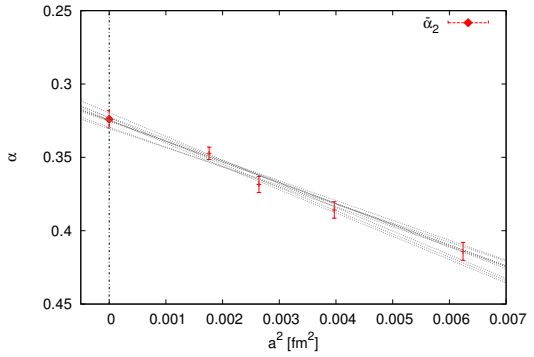

(b) without HYP, $\overline{\alpha}_2 = 0.324 \pm 0.006$

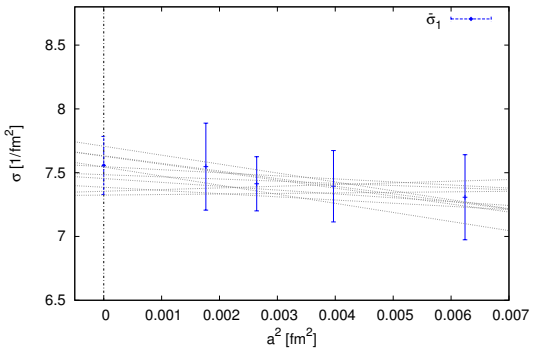

(c) HYP, $\overline{\sigma}_1 = (7.56 \pm 0.23) 1/\mathrm{fm}^2$

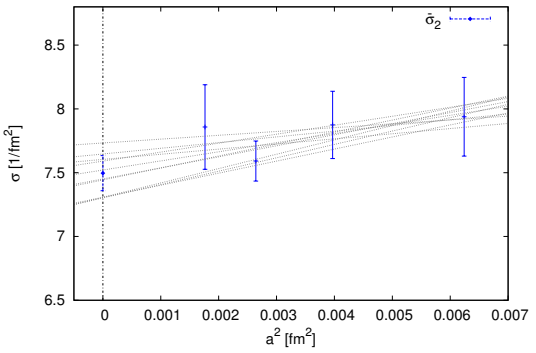

(d) without HYP, $\overline{\sigma}_2 = (7.50 \pm 0.14) 1/\mathrm{fm}^2$

Figure 6: Continuum extrapolations. **(a)** and **(c)** originate from HYP potential data and were extrapolated pairwise. The same for **(b)** and **(d)** which come from data without HYP.
The grey straight lines show randomly selected extrapolations out of 1000.

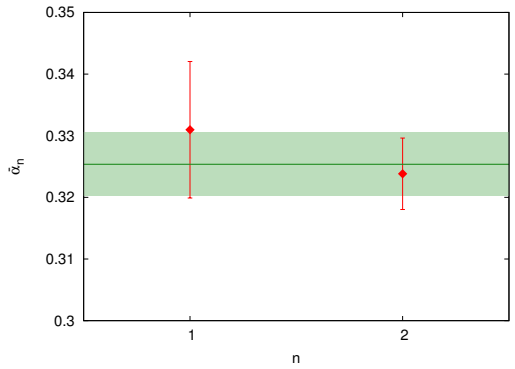

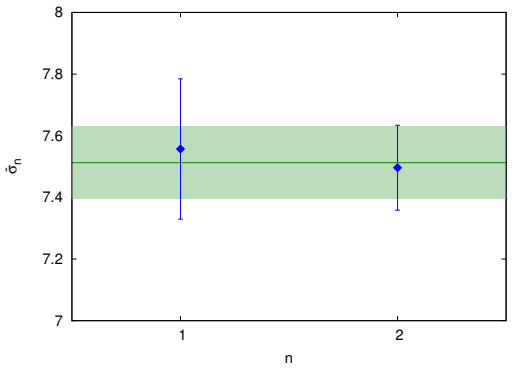

Figure 7: Merging of the results from the different data (HYP (1), without HYP (2)).

2.5 Final lattice potential

Throughout the last sections, we constructed an expression for the static $Q\overline{Q}$ potential that is based on lattice data from four different ensembles of gauge link configurations. Since we already extrapolated the potential model parameters to the continuum, one can directly generate further results with the help of the potential and no further extrapolations are necessary. The continuum expression should be valid in the typical lattice region starting from around 0.1 fm. The mean values and standard errors from the continuum list $\{(\alpha_i, \sigma_i)\}_{i=1...1000}$ yield the final continuum result:

$$\begin{aligned} \alpha &= 0.325 \pm 0.005 \\ \sigma &= (7.51 \pm 0.12)\frac{1}{\text{fm}^2} \\ \text{corr}(\alpha, \sigma) &= -0.65 \ . \end{aligned} \tag{2.22}$$

The potential $V_{\text{lat}}(r) = -\frac{\alpha}{r} + \sigma r$ is completely described by these five numbers in (2.22).

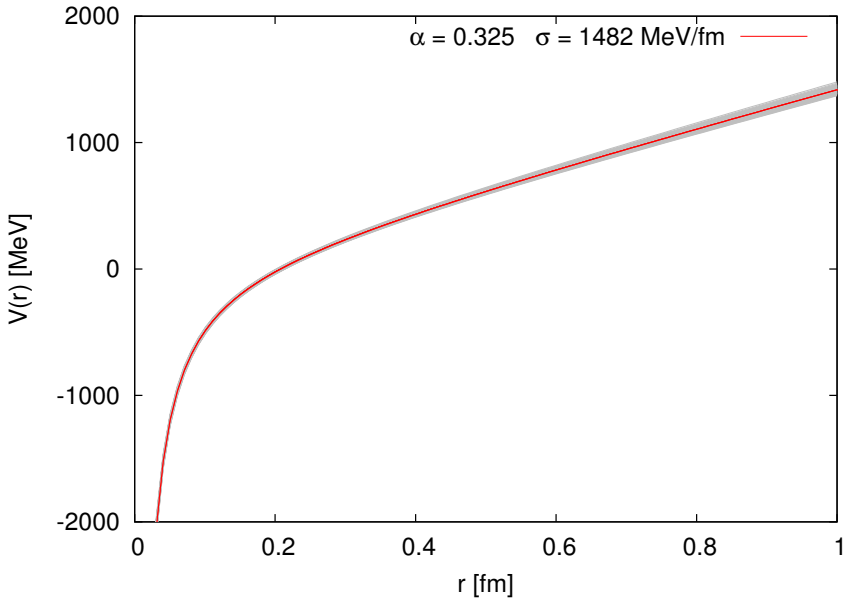

Figure 8: The final potential $V_{\text{lat}}(r) = -\frac{\alpha}{r} + \sigma r$ derived from lattice data. The grey band results from the $\{(\alpha_i, \sigma_i)\}_{i=1...1000}$ continuum pairs and can be interpreted as uncertainty.

The final errors in our results are statistical errors, and in case of σ we additionally included the errors of the lattice spacings. Other possible errors associated with the lattice computation, like finite volume effects and non-vanishing light quark masses, have

been neglected because their effects were found to be rather small [12,13].
For a cross-check of our results with ETMC analyses we calculate the Sommer parameter with equation (2.1),

$$r_0 = \sqrt{\frac{1.65 - \alpha}{\sigma}}, \tag{2.23}$$

and compare it to $r_0 = 0.420(14)$ fm, a value which is extrapolated to the continuum from [4]. We find $r_0 = 0.420(3)$ fm which is in total agreement.

3 Perturbative potential

3.1 Momentum space

Conventionally the static $Q\overline{Q}$ potential in perturbation theory for gauge group SU(3) is expressed in momentum space as

$$V_{\text{pert}}(p) = -\frac{16\pi}{3p^2}\alpha_V\left[\alpha_s(\mu), L\left(\frac{\mu}{p}\right)\right]. \tag{3.1}$$

where $L\left(\frac{\mu}{p}\right) = \ln\left(\frac{\mu^2}{p^2}\right)$. The specific choice of the renormalization scale μ has no impact on the static potential due to its renormalization group invariance. With the choice $\mu = p$ we gain $L(1) = 0$ and therewith α_V becomes a function of $\alpha_s(p)$ only. Adopting this specification, the static potential reads

$$V_{\text{pert}}(p) = -\frac{16\pi}{3p^2}\alpha_s(p)\left\{1 + \frac{\alpha_s(p)}{4\pi}a_1 + \left(\frac{\alpha_s(p)}{4\pi}\right)^2 a_2 + \left(\frac{\alpha_s(p)}{4\pi}\right)^3 \left[a_3 + a_{3\ln}\ln\alpha_s(p)\right]\right\}. \tag{3.2}$$

For $n_f = 2$ quark flavors and in the $\overline{MS}$ scheme the coefficients appearing in the above equation are known [3] as

$$a_1 = \frac{73}{9}, \qquad a_2 = \frac{25139}{162} + 9\pi^2\left(4 - \frac{\pi^2}{4}\right) + \frac{94}{3}\zeta(3), \tag{3.3}$$

$$a_3 = 8783.16(38), \qquad a_{3\ln} = 144\pi^2. \tag{3.4}$$

The running of the coupling parameter α_s is described by the definition of the QCD β-function

$$\beta[\alpha_s(\mu)] = \frac{\mu}{\alpha_s(\mu)}\frac{d\alpha_s(\mu)}{d\mu}, \tag{3.5}$$

whose perturbative expansion in α_s is presently known [10] as

$$\beta[\alpha_s] = -\frac{\alpha_s}{2\pi}\beta_0\left[1 + \frac{\alpha_s}{4\pi}b_1 + \left(\frac{\alpha_s}{4\pi}\right)^2 b_2 + \left(\frac{\alpha_s}{4\pi}\right)^3 b_3 + \left(\frac{\alpha_s}{4\pi}\right)^4 b_4 + \mathcal{O}(\alpha_s^5)\right]. \tag{3.6}$$

The constants, again for $n_f = 2$ and in the $\overline{MS}$ scheme, are given [11] as

$$\beta_0 = \frac{29}{3}, \qquad b_1 = \frac{230}{29}, \tag{3.7}$$

$$b_2 = \frac{48241}{522}, \qquad b_3 = \frac{18799309}{14094} + \frac{275524}{783}\zeta(3), \tag{3.8}$$

$$b_4 = \frac{2522305027}{112752} + \frac{109354687}{4698}\zeta(3) - \frac{68881}{1620}\pi^4 - \frac{16675240}{783}\zeta(5). \tag{3.9}$$

In order to extract an explicit value for $\alpha_s(\mu)$ equation (3.5) is integrated. This leads to an implicit expression for α_s,

$$\ln\left(\frac{\mu}{\Lambda_{QCD}}\right) = \frac{b_1}{2\beta_0}\ln\left(\frac{\beta_0\alpha_s(\mu)}{4\pi}\right) + \frac{2\pi}{\beta_0\alpha_s(\mu)} + \frac{1}{\beta_0}\int_0^{\alpha_s(\mu)}\frac{\mathrm{d}\alpha_s'}{\alpha_s'}\left(\frac{\beta_0}{\beta[\alpha_s']} + \frac{2\pi}{\alpha_s'} - \frac{b_1}{2}\right), \tag{3.10}$$

which can be further simplified and solved for α_s. Again one can choose $\mu = p$. Additionally, a new constant Λ_{QCD} appears from the integration. The interpretation of this external input parameter is the definition of a scale for perturbation theory, which is only valid for large momenta $p \gg \Lambda_{QCD}$. As well as some of the constants, the value of Λ_{QCD} depends on the renormalization scheme. Referring to the $\overline{MS}$-scheme we write $\Lambda_{\overline{MS}}$. A plot of $V_{\mathrm{pert}}(p)$ (3.2) at the highest order NNNLO is shown in figure 10.

3.2 Position space

Naturally, perturbation theory is done in momentum space. But for certain applications it is useful to transform the expression into position space. This can be done straightforwardly by applying the three dimensional Fourier transform:

$$V_{\mathrm{pert}}(r) = \int \frac{\mathrm{d}^3p}{(2\pi)^3}\mathrm{e}^{i\mathbf{pr}}V_{\mathrm{pert}}(p). \tag{3.11}$$

The problem that occurs with this transformation is the inclusion of momenta $p \lesssim \Lambda_{\overline{MS}}$ in the integration. However, in this region perturbation theory is no longer reliable which causes uncontrolled contributions to $V_{\mathrm{pert}}(r)$. Note that such uncontrolled contributions from outside the perturbative regime are also present in momentum space because of loop integrations $\int \frac{\mathrm{d}^4q}{(2\pi^4)}$ which naturally receive contributions from $p \lesssim \Lambda_{\overline{MS}}$ [3].
The problem in position space can be cured by restricting the Fourier integral to the perturbative momentum regime. Therefore a momentum cutoff $\mu_f > \Lambda_{\overline{MS}}$ is introduced. Conventionally, the corrected position space static potential is represented as

$$V_{\mathrm{pert}}(r,\mu_f) = V_{\mathrm{pert}}(r) - \delta V(r,\mu_f), \tag{3.12}$$

where the low momentum part

$$\delta V(r,\mu_f) = \int_{|\mathbf{p}|<\mu_f}\frac{\mathrm{d}^3p}{(2\pi)^3}\mathrm{e}^{i\mathbf{pr}}V_{\mathrm{pert}}(p) \tag{3.13}$$

is substracted. In the special case of $\mu_f = 0$, δV vanishes and we obtain the result of an ordinary Fourier transform. A compact representation for equations (3.11) and (3.13) has been derived in [3]. To this end, polynomials of degree k are introduced:

$$P_k(L) = \sum_{m=0}^{k}\rho_{km}L^m. \tag{3.14}$$

The dimensionless coefficients for $k \leq 3$ are: $\rho_{k0} = a_k$ (with $a_0 = 1$),

$$\rho_{21} = (2a_1 + b_1)\beta_0, \quad \rho_{31} = (3a_2 + 2a_1 b_1 + b_2)\beta_0, \quad \rho_{32} = (3a_1 + \frac{5}{2}b_1)\beta_0^2 \tag{3.15}$$

and $\rho_{kk} = \beta_0^k$.
With this notation the perturbative static $Q\overline{Q}$ potential in position space, resulting from a restricted Fourier transform, reads

$$\begin{aligned} V_{\text{pert}}(r) = -\frac{4}{3}\frac{\alpha_s(1/r)}{r}\Bigg\{1 + \frac{\alpha_s(1/r)}{4\pi}\Big(P_1(0) + 2\gamma_E P_1'\Big) \\ + \left(\frac{\alpha_s(1/r)}{4\pi}\right)^2\left[P_2(0) + 2\gamma_E P_2'(0) + \left(2\gamma_E^2 + \frac{\pi^2}{6}\right)P_2''\right] \\ + \left(\frac{\alpha_s(1/r)}{4\pi}\right)^3\Bigg[a_{3\ln}\ln\alpha_s + P_3(0) + 2\gamma_E P_3'(0) + \left(2\gamma_E^2 + \frac{\pi^2}{6}\right)P_3''(0) \\ + \frac{1}{3}\Big(\left(4\gamma_E^2 + \pi^2\right)\gamma_E + 8\zeta(3)\Big)P_3'''\Bigg]\Bigg\} \end{aligned} \tag{3.16}$$

and

$$\begin{aligned} \delta V(r,\mu_f) = -\frac{8}{3}\frac{\alpha_s(1/r)}{\pi}\mu_f\Bigg\{1 + \frac{\alpha_s(1/r)}{4\pi}\Big(P_1\Big(\ln\tfrac{1}{r^2\mu_f^2}\Big) + 2P_1'\Big) \\ + \left(\frac{\alpha_s(1/r)}{4\pi}\right)^2\left[P_2\Big(\ln\tfrac{1}{r^2\mu_f^2}\Big) + 2P_2'\Big(\ln\tfrac{1}{r^2\mu_f^2}\Big) + 4P_2''\right] \\ + \left(\frac{\alpha_s(1/r)}{4\pi}\right)^3\Bigg[a_{3\ln}\Big(\ln\alpha_s + \frac{1}{2}\ln\tfrac{1}{r^2\mu_f^2} + \frac{1}{2} - \gamma_E - \frac{r\mu_f}{\pi}\Big) + P_3\Big(\ln\tfrac{1}{r^2\mu_f^2}\Big) + 2P_3'\Big(\ln\tfrac{1}{r^2\mu_f^2}\Big) \\ + 4P_3''\Big(\ln\tfrac{1}{r^2\mu_f^2}\Big) + 8P_3'''\Bigg] + \mathcal{O}(r^2\mu_f^2)\Bigg\}. \end{aligned} \tag{3.17}$$

In position space we always specialize the renormalization scale to $\mu = \frac{1}{r}$, as already adopted in the equations above. At this point we need an explicit expression of α_s. Solving equation (3.10) approximately for α_s by expanding $\alpha_s(\mu)$ in powers of $1/l$, where $l \equiv L\left(\frac{\mu}{\Lambda_{\overline{MS}}}\right)$, and iteratively determining the expansion coefficients, results in

$$\begin{aligned} \alpha_s(\mu) = \frac{4\pi}{\beta_0 l}\Bigg\{1 - \frac{b_1}{\beta_0 l}\ln l + \Big(\frac{b_1}{\beta_0 l}\Big)^2\left[\ln^2 l - \ln l - 1 + \frac{b_2}{b_1^2}\right] \\ - \Big(\frac{b_1}{\beta_0 l}\Big)^3\left[\ln^3 l - \frac{5}{2}\ln^2 l - \Big(2 - \frac{3b_2}{b_1^2}\Big)\ln l + \frac{1}{2}\Big(1 - \frac{b_3}{b_1^3}\Big)\right] \\ + \Big(\frac{b_1}{\beta_0 l}\Big)^4\left[\ln^4 l - \frac{13}{3}\ln^3 l - \Big(\frac{3}{2} - 6\frac{b_2}{b_1^2}\Big)\ln^2 l + \Big(4 - 3\frac{b_2}{b_1^2} - 2\frac{b_3}{b_1^3}\Big)\ln l \right. \\ \left. + \frac{7}{6} - \frac{b_2}{b_1^2}\Big(3 - \frac{5}{3}\frac{b_2}{b_1^2}\Big) - \frac{1}{6}\frac{b_3}{b_1^3} + \frac{1}{3}\frac{b_4}{b_1^4}\right] + \mathcal{O}\Big(\frac{1}{l^5}\Big)\Bigg\}. \end{aligned} \tag{3.18}$$

Finally, equations (3.16), (3.17) and (3.18) together describe the perturbative static potential which is assumed to be reliable for $r \leq 1/\mu_f$. Figure 9 offers a visual impression for different cutoffs $\mu_f = \{3, 4, 5, 6\}\Lambda_{\overline{MS}} = \{906, 1208, 1510, 1812\}$ MeV. Beyond 0.2 fm the behaviour of the potentials starts to differ much and perturbation theory becomes decreasingly reliable. Moreover the convergence behaviour of $V_{\text{pert}}(r, \mu_f)$ for different perturbative orders in α_s is illustrated.

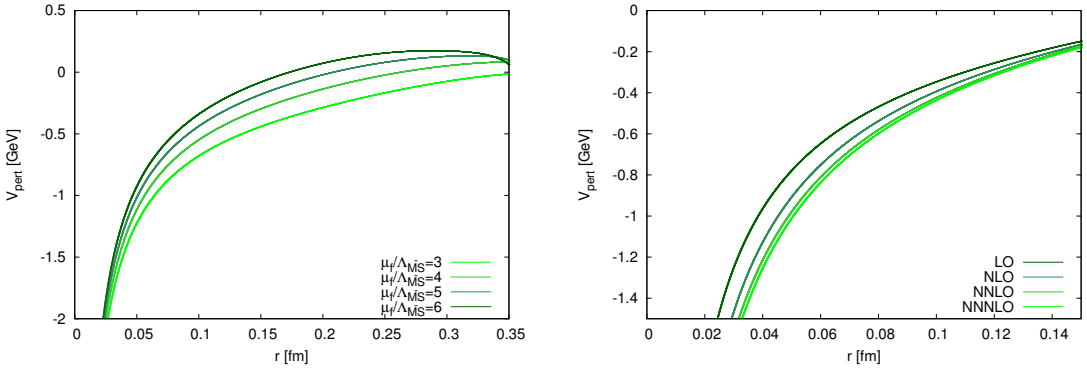

Figure 9: **Left**: The perturbative static potential for different values of μ_f.
Right: Convergence behaviour with changing orders LO up to NNNLO for $\mu_f = 5\Lambda_{\overline{MS}}$.

3.3 The parameter $\Lambda_{\overline{MS}}$

There is one open parameter which appears both in position and momentum space. It is $\Lambda_{\overline{MS}}$, which sets the scale in perturbation theory, but whose exact value is hard to determine within perturbation theory. This is why we have to make use of lattice data. Many calculations for determining the parameter have been done in the past [12, 13], which produced different values for $\Lambda_{\overline{MS}}$ depending on the strategy and the specific data. For reasons of transparency we determine the parameter on our own, with the same underlying data that we will use later for the calculation of the bottomonium system. Our technique, which is performed in momentum space, was developed in [14] and is used here in the same way. The major difference is, that we make use of the continuum expression of the lattice potential which we derived in chapter 2. For the further calculation we need this lattice continuum potential in momentum space. After a continuous Fourier transform of equation (2.15) it reads

$$V_{\text{lat}}(p) = \frac{4\pi\alpha}{p^2} - \frac{8\pi\sigma}{p^4}. \tag{3.19}$$

To summarize the technique, we compare the momentum space version of the perturbative potential (3.2) with $V_{\text{lat}}(p)$ in an area in which both expressions are reliable. $\Lambda_{\overline{MS}}$

comes in with equation (3.10) and is adjusted by minimizing the distance between both potentials in the area between $p_{\min}$ and $p_{\max}$. Figure 10 illustrates this procedure of fitting the two functions.
In order not to prefer a certain setup in the calculation and to prevent possible correlations we perform a huge number of fits. Thereby the setup is choosen randomly. What we obtain is a mean value for $\Lambda_{\overline{MS}}$ which can be interpreted as a final result. The standard deviation corresponds to the systematic error.
Concretely, we perform 20000 fits. In each fit the perturbative order NNLO or NNNLO, a parameter pair (α_i, σ_i) from the continuum list and a fit intervall $[p_{\min}, p_{\max}]$ with

- $p_{\min} \in [1500, 2250]$ MeV
- $p_{\max} \in [2250, 3000]$ MeV
- $p_{\max} - p_{\min} \geq 375$ MeV

is choosen randomly. There are also two different methods how to treat the integral in equation (3.10), either inserting (3.6) and performing the integration numerically (method (1)), or expanding the integrand and performing the integral analytically (method (2)). The latter strategy yields

$$\ln\left(\frac{p}{\Lambda_{\overline{MS}}}\right) = \frac{b_1}{2\beta_0}\ln\left(\frac{\beta_0\alpha_s(p)}{4\pi}\right) + \frac{2\pi}{\beta_0\alpha_s(p)} + \frac{b_2 - b_1^2}{2\beta_0}\frac{\alpha_s(p)}{4\pi} + \frac{b_3 - 2b_1b_2 + b_1^3}{4\beta_0}\left(\frac{\alpha_s(p)}{4\pi}\right)^2 + \frac{b_4 - b_2^2 - 2b_1b_3 + 3b_1^2b_2 - b_1^4}{6\beta_0}\left(\frac{\alpha_s(p)}{4\pi}\right)^3 \quad (3.20)$$

They provide compatible results. Half of the fits are done with method (1) and the remaining ones with method (2). We finally obtain

$$\Lambda_{\overline{MS}} = 302(12) \text{ MeV}, \quad (3.21)$$

which will be used as in input throughout the upcoming calculations. Compared to the former result $\Lambda_{\overline{MS}} = 329(20)$ MeV in [14], (3.21) is $\approx 8\%$ smaller. This can be attributed to the continuum extrapolation, which is missing in [14].

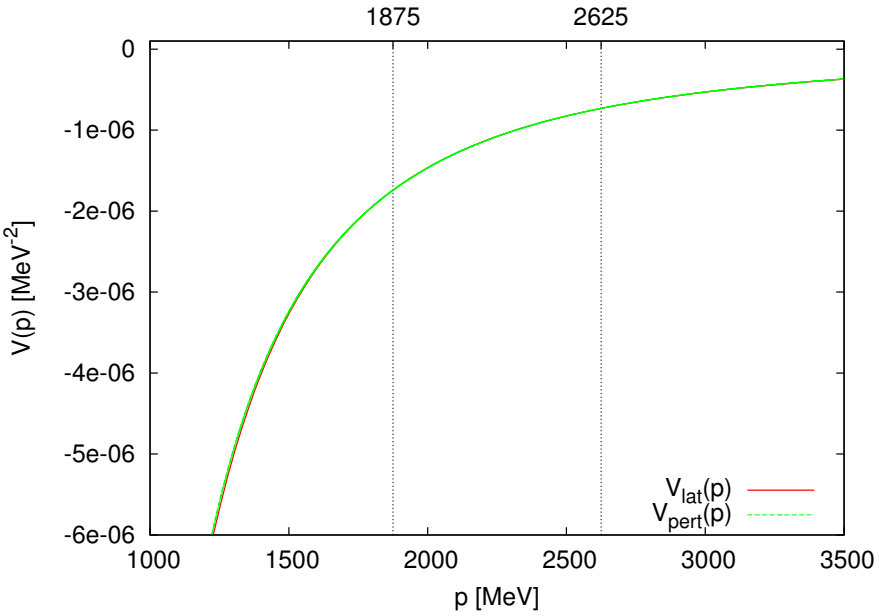

Figure 10: An illustration of the method to determine $\Lambda_{\overline{MS}}$. V_{lat} and V_{pert} are matched in a suitable area in momentum space in such a way that their distance is minimal. For the shown setup [NNNLO, method (2), $p_{\text{min}} = 1875$ MeV, $p_{\text{max}} = 2625$ MeV], the result is $\Lambda_{\overline{MS}} = 290$ MeV.

4 Combined potential

In the previous sections two expressions for the $Q\overline{Q}$ potential in position space have been derived. The first one V_{pert} from perturbation theory which can be used up to $r \ll \frac{1}{\Lambda_{\overline{MS}}}$ and V_{lat} from lattice QCD which is valid from $r \approx 0.1$ fm. Since we aim at constructing a position space potential that is applicable over the whole distance range, both expressions will be merged. The requirement, that the ranges of validity have an overlap is fulfilled. In order to have the full control we prescribe the distance where the transition takes place. According to the ranges of validity of the potentials we choose the transition area between 0.08 fm $\leq r \leq$ 0.20 fm. There are different strategies how to combine both potentials V_{pert} and V_{lat}. The easiest possibility is to join the two potentials together at a given distance, for instance $r_t = 0.15$ fm, so that the full potential reads

$$V(r) = \begin{cases} V_{\text{pert}}(r), & r < r_t \\ V_{\text{lat}}(r), & r \geq r_t \end{cases} . \tag{4.1}$$

Since the overall energy constant of the potential is not important, both expressions can always be shifted to achieve $V_{\text{lat}}(r_t) = V_{\text{pert}}(r_t)$. The disadvantage of this solution is, that at the transition point the potential is no longer smooth because the first derivative is not necessarily continuous. Although we found compatible results with this option, (4.1) will not be used in our final analysis.
Another strategy is inspired by the aim to have a smooth potential. We construct a third function $V_{\text{trans}}(r)$ that interpolates between the two potentials. At the transition points r_1 and r_2, which we prescribe, the first derivatives coincide. The simplest choice for this interpolating function is a quadratic function

$$V_{\text{trans}}(r) = ar^2 + br + c, \tag{4.2}$$

whose parameters are fixed by the following boundary conditions at the transition points:

$$\begin{aligned} V_0 + V_{\text{pert}}(r_1) &= V_{\text{trans}}(r_1) \\ V_{\text{lat}}(r_2) &= V_{\text{trans}}(r_2) \\ \left.\frac{\mathrm{d}V_{\text{pert}}}{\mathrm{d}r}\right|_{r=r_1} &= \left.\frac{\mathrm{d}V_{\text{trans}}}{\mathrm{d}r}\right|_{r=r_1} \\ \left.\frac{\mathrm{d}V_{\text{lat}}}{\mathrm{d}r}\right|_{r=r_2} &= \left.\frac{\mathrm{d}V_{\text{trans}}}{\mathrm{d}r}\right|_{r=r_2} . \end{aligned} \tag{4.3}$$

Solving these four linear equations yields a, b, c and the constant energy shift V_0, which we added to the perturbative potential. In this case the full potential reads

$$V(r) = \begin{cases} V_0 + V_{\text{pert}}(r), & r < r_1 \\ V_{\text{trans}}(r), & r_1 \leq r \leq r_2 \\ V_{\text{lat}}(r), & r \geq r_2 \end{cases} . \tag{4.4}$$

Since there is one open parameter μ_f left in the perturbative expression, it would be also possible to merge the two potentials by fixing this parameter under the condition that the derivatives of the potentials have to be continuous at only one given transition point. Thus we would avoid the interpolation. But this is not necessarily the case or would lead to too large values for μ_f. During the numerical analysis we will vary the parameter in an appropriate area.
There are more parameters that influence the exact shape of the combined potential. When using the potential in a computation one has to do a statistical analysis by repeating the computation many times with different input parameters. The following quantities are randomly choosen:

- $\mu_f \in [3.0, 7.0]\ \Lambda_{\overline{MS}}$
- $\Lambda_{\overline{MS}}$ from a Gaussian distribution with $\overline{\Lambda}_{\overline{MS}} = 302$ MeV and $\Delta\Lambda_{\overline{MS}} = 12$ MeV
- $r_1 \in [0.08, 0.12]$ fm
- $r_2 \in [0.16, 0.20]$ fm
- a pair (α, σ) from a 2-dimensional Gaussian distribution (characterized by (2.22))

Since we want to investigate the influence of string breaking to the bottomonium system in chapter 5, we introduce another expression:

$$V(r) = \begin{cases} V_0 + V_{\text{pert}}(r), & r < r_1 \\ V_{\text{trans}}(r), & r_1 \leq r \leq r_2 \\ V_{\text{lat}}(r), & r_2 \leq r < r_{sb} \\ V_{\text{lat}}(r_{sb}), & r \geq r_{sb} \end{cases} , \tag{4.5}$$

with $V_{\text{lat}}(r_{sb}) = \text{const}$. For the string breaking distance $r_{sb} = 1.13(10)(10)$ fm we refer to [15]. Figure 11 illustrates the introduced combination strategies.

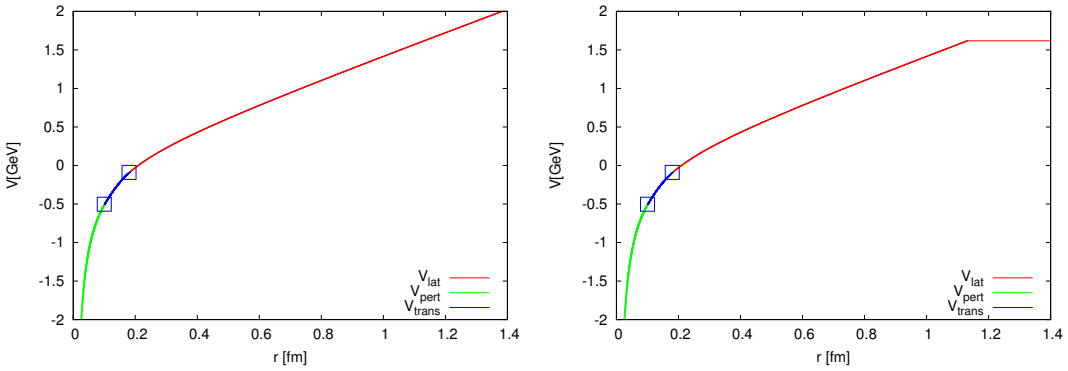

(a) Merging by interpolation between $r_1 = 0.1$ fm and $r_2 = 0.18$ fm.

(b) Adding string breaking at $r = 1.13$ fm [15].

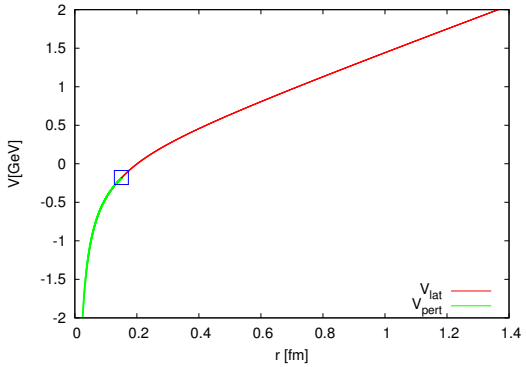

(c) Special case with only one transition point at $r_t = 0.15$ fm.

Figure 11: Different strategies to combine V_{pert} and V_{lat}. In the perturbative formulas μ_f was set to $\mu_f = 5 \times 302$ MeV.

5 Bottomonium spectrum

5.1 Solving the Schrödinger equation

As an application of our combined static $Q\overline{Q}$ potential in position space which is valid across the whole distance range, we use it to reproduce the bottomonium system in the static limit. Since bottomonium is the least relativistic mesonic system and several $b\bar{b}$ states are experimentally established, it is well suited to test the potential.
The spectrum is determined by solving the non-relativistic Schrödinger equation ($\hbar = 1$)

$$\left[-\frac{1}{2m}\Delta + V(r)\right]\psi(r) = E\psi(r) \tag{5.1}$$

with the spherically symmetric potential $V(r)$ according to equation (4.4) or (4.5). $m = \frac{m_b}{2}$ is the reduced mass of the two interacting quarks with masses m_b. With the introduction of polar coordinates (r, θ, ϕ) the Laplacian operator Δ reads

$$\Delta = \frac{1}{r^2}\frac{\partial}{\partial r}\left(r^2\frac{\partial}{\partial r}\right) + \frac{1}{r^2\sin\theta}\frac{\partial}{\partial\theta}\left(\sin\theta\frac{\partial}{\partial\theta}\right) + \frac{1}{r^2\sin^2\theta}\frac{\partial^2}{\partial\phi^2}. \tag{5.2}$$

We can identify the polar representation of the squared angular momentum operator

$$L^2 = -\left[\frac{1}{\sin\theta}\frac{\partial}{\partial\theta}\left(\sin\theta\frac{\partial}{\partial\theta}\right) + \frac{1}{\sin^2\theta}\frac{\partial^2}{\partial\phi^2}\right] \tag{5.3}$$

in equation (5.2). The Schrödinger equation now reads

$$\left[-\frac{1}{2m}\left(\frac{1}{r^2}\frac{\partial}{\partial r}\left(r^2\frac{\partial}{\partial r}\right) - \frac{L^2}{r^2}\right) + V(r)\right]\psi(r,\theta,\phi) = E\psi(r,\theta,\phi). \tag{5.4}$$

A separation of variables with the ansatz

$$\psi(r,\theta,\phi) = R(r)Y(\theta,\phi) \tag{5.5}$$

splits the Schrödinger equation into an angular and a radial equation. The solutions of the angular equation are the well-known spherical harmonics $Y_{\ell m}(\theta,\phi)$ that are eigenstates of L^2:

$$L^2 Y_{\ell m}(\theta,\phi) = \ell(\ell+1)Y_{\ell m}(\theta,\phi), \tag{5.6}$$

with integer numbers $\ell \geq 0$ and $m = -\ell, ..., \ell$.
The radial equation then reads

$$-\frac{1}{2m}\frac{1}{r^2}\frac{\partial}{\partial r}\left(r^2\frac{\partial R_{n\ell}}{\partial r}\right) + \left[V(r) + \frac{\ell(\ell+1)}{2mr^2}\right]R_{n\ell}(r) = E_{n\ell}R_{n\ell}(r). \tag{5.7}$$

The energy $E_{n\ell}$ will depend on ℓ because of the effective potential (5.9). Moreover the index n indicates the quantization of the bound states.
With the substitution $u_{n\ell}(r) = rR_{n\ell}(r)$ and after some algebra [16] we find

$$-\frac{1}{2m}\frac{\mathrm{d}^2 u_{n\ell}}{\mathrm{d}r^2} + \left[V(r) + \frac{\ell(\ell+1)}{2mr^2} - E_{n\ell}\right] u_{n\ell}(r) = 0, \tag{5.8}$$

which is analogous to the Schrödinger equation in one dimension with an effective potential

$$V_{\text{eff}}(r) = V(r) + \frac{\ell(\ell+1)}{2mr^2}. \tag{5.9}$$

The complete wave function

$$\psi_{n\ell m}(r,\theta,\phi) = R_{n\ell}(r)Y_{\ell m}(\theta,\phi) \tag{5.10}$$

has to fulfill the normalization condition. The spherical harmonics themselves are already normalized by definition. As a consequence we find that $u_{n\ell}(r)$ needs to be normalized as well:

$$\int_0^\infty |u_{n\ell}(r)|^2 dr = 1. \tag{5.11}$$

To ensure the normalization, the function $u_{n\ell}(r)$ has to vanish for large r. This can be formulated as a boundary condition:

$$r \to \infty: \quad u_{n\ell}(r) \longrightarrow 0. \tag{5.12}$$

To get an idea of the wavefunction's behaviour and the boundary conditions we take a look at the asymptotic behaviour. The behaviour for $r \to 0$ is determined by

$$\frac{\mathrm{d}^2 u_{n\ell}}{\mathrm{d}r^2} \simeq \frac{\ell(\ell+1)}{r^2} u_{n\ell}(r), \tag{5.13}$$

yielding the solution

$$r \to 0: \quad u_{n\ell}(r) \sim r^{\ell+1}. \tag{5.14}$$

Looking at $r \to \infty$ the Schrödinger equation is dominated by the linear rising part σr. The resulting asymptotic differential equation

$$\frac{\mathrm{d}^2 u_{n\ell}}{\mathrm{d}r^2} \simeq \frac{\sigma r}{2m} u_{n\ell}(r) \tag{5.15}$$

is known as Airy equation. To guarantee the boundary condition (5.12), the solution is the Airy function of the first kind [17]:

$$u_{n\ell}(r) \simeq \mathrm{Ai}\left(r\sqrt[3]{\frac{\sigma}{2m}}\right). \tag{5.16}$$

Solving the Schrödinger equation yields the binding energy of a bound state $E_{n\ell}$ and the corresponding wave function $u_{n\ell}$. Inserting $\ell = 0$ gives the S-states of the system, respectively $\ell = 1$ the P-states.
To actually gain the masses $M_{n\ell}$ of the bottomonium states, the quark masses have to be added to the binding energies [1]: $M_{n\ell} = E_{n\ell} + 2m_b$. Because the overall energy constant to $V(r)$ is still arbitrary, absolute values of $E_{n\ell}$ are not meaningful. We can only interpret energy differences ΔE between the states. For a proper comparison with experimental states we fix $M^*_{10} \equiv m_{\text{exp}}(\eta_b(1S)) = 9.399$ GeV and obtain any other state by adding the energy difference between the state and the $1S$ result. Concretely the calibrated states are calculated by

$$M^*_{n\ell} = M^*_{10} + \Delta E_{n\ell}, \tag{5.17}$$

with $\Delta E_{n\ell} \equiv E_{n\ell} - E_{10}$ and $\Delta E_{10} = 0$.

5.2 Numerical setup

Equation (5.8) can be solved with the same methods one uses in one dimension. As we deal with a two point boundary value problem, the shooting method is applied [18]. Schematically, the differential equation is integrated over an interval $[r_{\text{min}}, r_{\text{max}}]$ satisfying the boundary condition at the starting point r_{max}. At the endpoint r_{min} the second boundary condition is not necessarily satisfied. The deviations from the desired boundary condition are used to adapt the starting conditions until both boundary conditions are fulfilled. This is numerically realized by an iterative root finding procedure with a Runge-Kutta method in each step. The energy $E_{n\ell}$, which is a part of the starting conditions, is improved up to an arbitrary numerical precision. The reason for starting the integration from $r_{\text{max}} > r_{\text{min}}$ is to avoid an exponential increase of the wave function, which appears when doing it the other way round. From equation (5.14) we can specify the boundary conditions at the endpoint:

$$\begin{aligned} \ell = 0: &\qquad u_{n0}(r) \sim r \\ \ell = 1: &\qquad u_{n1}(r) \sim r^2 \ . \end{aligned} \tag{5.18}$$

To enable a numerical treatment, they (and equation (5.12)) can be formulated as

$$\begin{aligned} \ell = 0: &\qquad \tfrac{u_{n0}(r_{\text{min}}+\epsilon) - u_{n0}(r_{\text{min}})}{\epsilon} - \tfrac{u_{n0}(r_{\text{min}})}{r_{\text{min}}} = 0 \\ \ell = 1: &\qquad \tfrac{u'_{n1}(r_{\text{min}}+\epsilon) - u'_{n1}(r_{\text{min}})}{\epsilon} - \tfrac{u'_{n1}(r_{\text{min}})}{r_{\text{min}}} = 0 \\ &\qquad u_{n\ell}(r_{\text{max}}) \approx 0 \ . \end{aligned} \tag{5.19}$$

The numerical parameters r_{min}, r_{max} and the step size ϵ remain constant throughout the calculations. We checked that improving these parameters (smaller r_{min} or larger r_{max})

has no noticeable influence on the results.
Beside the numerical and the physical parameters, which we will vary in our final analysis as explained in chapter 4, there is one unspecified quantity left, the bottom quark mass m_b. Quark masses cannot be directly measured due to confinement. Their theoretical calculation is nontrivial and leads to a dependence on the underlying renormalization scheme. We decided to work with two different masses: the $\overline{MS}$-mass $m_{\overline{MS}} = 4.18$ GeV [19] and a mass from quark models $m_{\text{qm}} = 4.977$ GeV taken from [20]. Moreover we want to investigate the influence of string breaking by using equation (4.5). Altogether we do investigations for the following 3 setups:

- **(A)**: $m_b = m_{\overline{MS}}$, without string breaking (4.4)
- **(B)**: $m_b = m_{\text{qm}}$, without string breaking (4.4)
- **(C)**: $m_b = m_{\text{qm}}$, with string breaking (4.5)

From this analysis we get a first idea of the effect of different quark masses and string breaking on the bottomonium system.

5.3 Numerical results

A statistical analysis has been performed according to chapter 4. We performed $N_c = 3000$ computations for each state. The mean values and standard deviations of the energy differences give us the final results listed in table 4. Figure 12 illustrates the corresponding wave functions $u_{n\ell}(r)$. If necessary, the complete physical wave function $\psi_{n\ell m}$ can be obtained from equation (5.10).

		(A)	(B)	(C)
$\ell = 0$	ΔE_{20}	0.600 ± 0.005	0.584 ± 0.006	0.584 ± 0.006
	ΔE_{30}	1.036 ± 0.009	1.002 ± 0.009	1.003 ± 0.010
	ΔE_{40}	1.408 ± 0.012	1.356 ± 0.012	$1.173 \pm 0.019^*$
$\ell = 1$	ΔE_{11}	0.423 ± 0.007	0.419 ± 0.008	0.418 ± 0.007
	ΔE_{21}	0.880 ± 0.009	0.856 ± 0.009	0.855 ± 0.008
	ΔE_{31}	1.265 ± 0.012	1.221 ± 0.012	$1.173 \pm 0.015^*$

Table 4: Numerical results for the energy differences in units of GeV for 3 different setups (A), (B) and (C).

Below the results for the $b\bar{b}$ spectrum are shown in graphical form (figures 13 and 14). The states are calibrated in such a way, that the lowest state ($1S$) fits to the experimental value of the $\eta_b(1S)$ state. A comparison of the absolute masses to experimental values is shown in table 5. With our static approach the particular states which differ in spin cannot be reproduced. Nevertheless, the results are satisfying since many states are roughly reproduced. Especially the lower states are close to the experimental ones. The higher the states, the more discrepancies appear. There is also an obvious influence of the bottom quark mass. Results with the bigger mass $m_b = 4.977$ GeV from quark models (B) are located closer to the experimental states than those with the $\overline{MS}$-mass (A). With the addition of string breaking (C) the $B\overline{B}$-threshold ($m_{B\overline{B}} \approx 10.56$ GeV) is reproduced. The corresponding numerical results in table 4 are marked by *. The $4S$ and $3P$ states become meaningless in this case because the numerical values were located above the threshold before the addition of string breaking. An influence of string breaking on the states lower than the $B\overline{B}$-threshold is not observable.
To draw a comparison, one can have a look at the static results in [21]. Their results appear compatible with ours. For $3S$ and $1P$ they generated results slightly closer to the experimental values, but there are larger discrepancies with the $1S$ state. They did not investigate string breaking, but in a second step, relativistic corrections of order $1/m$ and a phenomenologically term, which causes hyperfine effects, were added. With the latter additions, the complete bottomonium spectrum below the $B\overline{B}$-threshold could be reproduced. We plan to improve our results in a similar way.

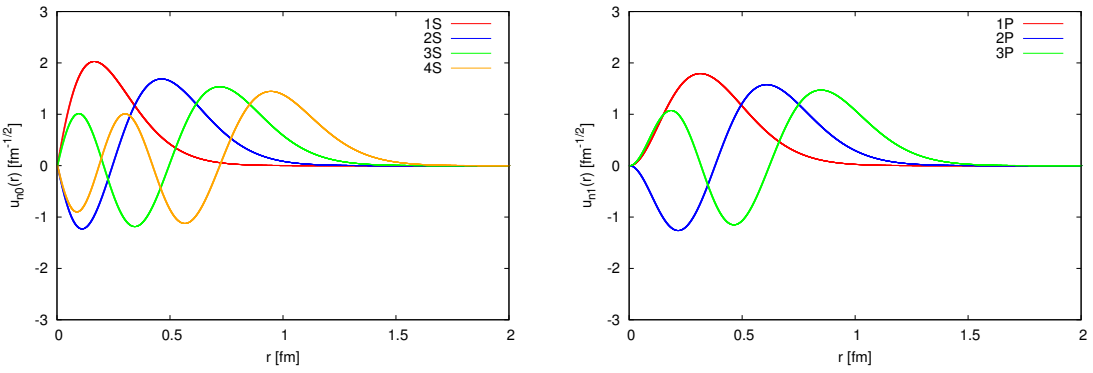

Figure 12: The normalized wave functions $u_{n\ell}(r)$ for setup (B).

	$n^{2S+1}L_J$	PDG	(A)	(B)	(C)
$\eta_b(1S)$	1^1S_0	9.399(3)	9.399(3)	9.399(3)	9.399(3)
$\Upsilon(1S)$	1^3S_1	9.4603(3)			
$h_b(1P)$	1^1P_1	9.8993(8)	9.822(8)	9.818(9)	9.817(8)
$\chi_{b0}(1P)$	1^3P_0	9.8594(5)			
$\chi_{b1}(1P)$	1^3P_1	9.8928(4)			
$\chi_{b2}(1P)$	1^3P_2	9.9122(4)			
$\eta_b(2S)$	2^1S_0	9.999(4)	9.999(6)	9.983(7)	9.983(7)
$\Upsilon(2S)$	2^3S_1	10.0233(3)			
$h_b(2P)$	2^1P_1	10.2598(12)	10.279(9)	10.255(9)	10.254(9)
$\chi_{b0}(2P)$	2^3P_0	10.2325(6)			
$\chi_{b1}(2P)$	2^3P_1	10.2555(6)			
$\chi_{b2}(2P)$	2^3P_2	10.2687(6)			
$\Upsilon(3S)$	3^3S_1	10.3552(5)	10.435(9)	10.401(9)	10.402(10)
$\chi_{b1}(3P)$	3^3P_1	10.5121(23)	10.664(12)	10.620(12)	-
$\Upsilon(4S)$	4^3S_1	10.5794(12)	10.807(3)	10.755(3)	-

Table 5: Absolute masses of the $b\bar{b}$-states for 3 different numerical setups are compared to experimental values [19]. The numerical results can be interpreted as spin-weighted averages. All masses are stated in units of GeV. $1S$ numerical results are fixed to 9.399 GeV.

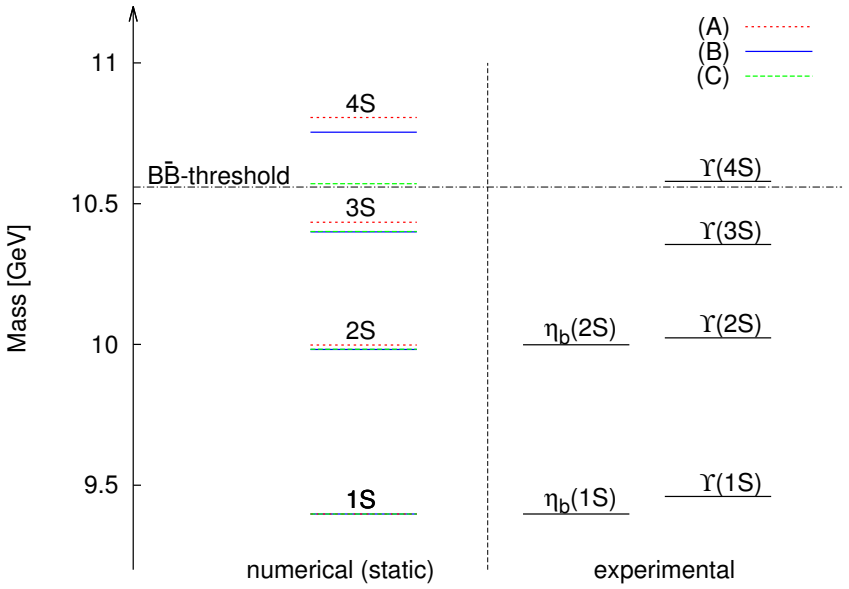

Figure 13: S-states ($\ell = 0$) of the bottomonium system in the static limit.

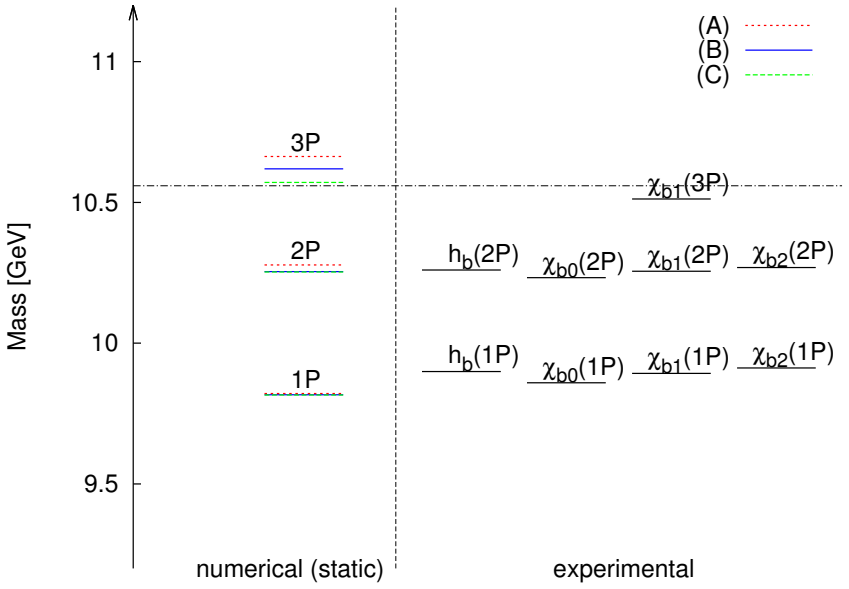

Figure 14: P-states ($\ell = 1$) of the bottomonium system in the static limit.

6 Conclusion and Outlook

In this work a full expression for the static quark-antiquark potential for $n_f = 2$ in position space was constructed. The short range part comes from perturbation theory and was obtained by a restricted Fourier transform into position space, whereas the long distance part was derived from lattice theory. In the latter case we fitted the Cornell potential to lattice data from four different ensembles and extrapolated the fitting parameters into the continuum. This was done for potential data without HYP smearing and, independently, for another data set with HYP smearing which extends to larger distances. In the continuum the results for the fitting parameters from both data sets were combined. The perturbative potential and the expression for the continuum lattice potential were merged by an interpolating function. As a first application of the combined potential, it was used to calculate the bottomonium spectrum in the static limit. Especially the systematics were investigated. The results are rather stable when changing the different input parameters. The addition of string breaking did not improve the numerical results for the bottomonium states, but reproduced the $B\overline{B}$-threshold.
In the future there are many other applications possible. For example, concerning bottomonium one can consider relativistic corrections for the non-infinite bottom quark mass. This is usually done by adding more terms to the potential. The expansion of the potential in inverse powers of the quark mass [22] reads

$$V(r) = V^{(0)}(r) + \frac{2}{m}V^{(1)}(r) + \frac{4}{m^2}V^{(2)}(r) + \mathcal{O}(1/m^3). \tag{6.1}$$

The term $V^{(1)}$ contains corrections of $\mathcal{O}(1/m)$ and $V^{(2)}$ contributes spin-dependent terms. Applying the latter correction should resolve states with different spin. Although the addition of these terms to the static potential seems to be straightforward, their computation is very challenging.

References

[1] Andrew Chisholm. *Measurements of the χ_c and χ_b Quarkonium States in pp Collisions with the ATLAS Experiment*, volume 1. Springer International Publishing, 2015.

[2] Jorge Segovia, Pablo G. Ortega, David R. Entem, and Francisco Fernández. Bottomonium spectrum revisited. *Phys. Rev.*, D93(7):074027, 2016.

[3] Felix Karbstein. Quark-antiquark static energy from a restricted Fourier transform. *JHEP*, 04:144, 2014.

[4] Remi Baron, Phillip Boucaud, Petros Dimopoulos, Roberto Frezzotti, David Palao, Giancarlo Rossi, Federico Farchioni, Gernot Münster, Tobias Sudmann, Vicent Gimenez, et al. Light meson physics from maximally twisted mass lattice QCD. *Journal of High Energy Physics*, 2010(8):1–41, 2010.

[5] H. J. Rothe. *Lattice Gauge Theories - An Introduction*, volume 74. World Scientific Lecture Notes in Physics, 2005.

[6] Yuri Makeenko. A Brief Introduction to Wilson Loops and Large N. *Phys. Atom. Nucl.*, 73:878–894, 2010.

[7] Michael Peardon, Francesco Knechtli, Michael Günther. *Lattice Quantum Chromodynamics: Practical Essentials*, volume 1. Springer Netherlands, 2016.

[8] Anna Hasenfratz and Francesco Knechtli. Flavor symmetry and the static potential with hypercubic blocking. *Phys. Rev.*, D64:034504, 2001.

[9] Philipp Werner, James Gubernatis, Naoki Kawashima. *Quantum Monte Carlo Methods - Algorithms for Lattice Models*, volume 1. Cambridge University Press, 2016.

[10] P. A. Baikov, K. G. Chetyrkin, and J. H. Kühn. Five-Loop Running of the QCD coupling constant. *Phys. Rev. Lett.*, 118(8):082002, 2017.

[11] Felix Karbstein. *private notes/unpublished.*

[12] Felix Karbstein, Antje Peters, and Marc Wagner. $\Lambda_{\overline{MS}}^{n_f=2}$ from a momentum space analysis of the quark-antiquark static potential. *Journal of High Energy Physics*, 2014(9):1–28, 2014.

[13] Karl Jansen, Felix Karbstein, Attila Nagy, and Marc Wagner. $\Lambda_{\bar{M}S}$ from the static potential for QCD with $n_f = 2$ dynamical quark flavors. *JHEP*, 01:025, 2012.

[14] Michelle Weber. $\Lambda_{\overline{MS}}$ aus dem statischen Quark-Antiquark Potential im Impulsraum. Bachelor Thesis, Goethe-Universität Frankfurt am Main, 2014.

[15] Gunnar S Bali, Hartmut Neff, Thomas Duessel, Thomas Lippert, Klaus Schilling, SESAM collaboration, et al. Observation of string breaking in QCD. *Physical Review D*, 71(11):114513, 2005.

[16] Wolfgang Nolting. *Grundkurs Theoretische Physik 5/2 - Quantenmechanik - Methoden und Anwendungen*, volume 6. Springer-Verlag Berlin Heidelberg, 2006.

[17] Richard L Hall and Nasser Saad. Schrödinger spectrum generated by the cornell potential. *Open Physics*, 13(1), 2015.

[18] William H. Press, Saul A. Teukolsky, William T. Vetterling, and Brian P. Flannery. *Numerical Recipes in C: The Art of Scientific Computing.* Cambridge University Press, 2007.

[19] C. Patrignani et al. Review of Particle Physics. *Chin. Phys.*, C40(10):100001, 2016.

[20] Stephen Godfrey and Nathan Isgur. Mesons in a relativized quark model with chromodynamics. *Physical Review D*, 32(1):189, 1985.

[21] Alexander Laschka, Norbert Kaiser, and Wolfram Weise. Quark-antiquark potential to order $1/m$ and heavy quark masses. *Phys. Rev. D*, 83:094002, May 2011.

[22] Yoshiaki Koma, Miho Koma, and Hartmut Wittig. Relativistic corrections to the static potential at $\mathcal{O}(1/m)$ and $\mathcal{O}(1/m^2)$. *PoS*, LAT2007:111, 2007.

Erklärung

Nach § 30 (12) der Prüfungsordnung für den Bachelor- und Masterstudiengang Physik der Johann-Wolfgang-Goethe-Universität Frankfurt am Main versichere ich, dass ich die vorliegende Arbeit selbstständig und ohne Benutzung anderer als der angegebenen Quellen und Hilfsmittel verfasst habe. Alle Stellen der Arbeit, die wörtlich oder sinngemäß aus Veröffentlichungen oder aus anderen fremden Texten entnommen wurden, sind als solche kenntlich gemacht. Weiter erkläre ich, dass die Arbeit nicht, auch nicht auszugsweise, für eine andere Prüfungs- oder Studienleistung verwendet worden ist.

Frankfurt am Main, 24.03.2017

Michelle Weber